Evaluation of MJO Forecast Skill from Several Statistical and Dynamical Forecast Models

KYONG-HWAN SEO

Division of Earth Environmental System, Pusan National University, Busan, South Korea

WANQIU WANG, JON GOTTSCHALCK, QIN ZHANG, JAE-KYUNG E. SCHEMM, WAYNE R. HIGGINS, AND ARUN KUMAR

Climate Prediction Center, NOAA/NWS/NCEP, Camp Springs, Maryland

(Manuscript received 10 January 2008, in final form 15 October 2008)

ABSTRACT

This work examines the performance of Madden–Julian oscillation (MJO) forecasts from NCEP's coupled and uncoupled general circulation models (GCMs) and statistical models. The forecast skill from these methods is evaluated in near–real time. Using a projection of El Niño–Southern Oscillation (ENSO)-removed variables onto the principal patterns of MJO convection and upper- and lower-level circulations, MJO-related signals in the dynamical model forecasts are extracted. The operational NCEP atmosphere–ocean fully coupled Climate Forecast System (CFS) model has useful skill (>0.5 correlation) out to ~15 days when the initial MJO convection is located over the Indian Ocean. The skill of the CFS hindcast dataset for the period from 1995 to 2004 is nearly comparable to that from a lagged multiple linear regression model, which uses information from the previous five pentads of the leading two principal components (PCs). In contrast, the real-time analysis for the MJO forecast skill for the period from January 2005 to February 2006 using the lagged multiple linear regression model is reduced to ~10–12 days. However, the operational CFS forecast for this period is skillful out to ~17 days for the winter season, implying that the coupled dynamical forecast has some usefulness in predicting the MJO compared to the statistical model.

It is shown that the coupled CFS model consistently, but only slightly, outperforms the uncoupled atmospheric model (by one to two days), indicating that only limited improvement is gained from the inclusion of the coupled air–sea interaction in the MJO forecast in this model. This slight improvement may be the result of the existence of a propagation barrier around the Maritime Continent and the far western Pacific in the NCEP Global Forecast System (GFS) and CFS models, as shown in several previous studies. This work also suggests that the higher horizontal resolution and finer initial data might contribute to improving the forecast skill, presumably as a result of an enhanced representation of the Maritime Continent region.

1. Introduction

The Madden–Julian oscillation (MJO) is the most prominent physical mode of tropical intraseasonal variability in the atmosphere (Madden and Julian 1994). The MJO not only influences the weather and climate of the global tropical regions but also affects precipitation and circulation patterns in extratropical regions through teleconnections. For example, the strong tropical upper tropospheric divergence and subtropical convergence induced by enhanced MJO convection over the warm tropical ocean in the Eastern Hemisphere act as a wave source, generating the northward propagating stationary Rossby wave train (Matthews et al. 2004; Lin et al. 2006) and therefore modulating the midlatitude jet streams. Strong enhanced convection located over the west Pacific is linked with rainfall variability along western North America (e.g., Mo and Higgins 1998; Higgins et al. 2000; Whitaker and Weickmann 2001). In fact, rainfall variations over almost all global regions (Donald et al. 2006) seem to be related to the circulation change.

The MJO is also associated with the global monsoon systems that occur in Asia, Australia, and the Americas

Corresponding author address: Dr. Kyong-Hwan Seo, Division of Earth Environmental System, Pusan National University, Busan 609-735, South Korea.
E-mail: khseo@pusan.ac.kr

DOI: 10.1175/2008JCLI2421.1

(e.g., Yasunari 1980; Lau and Chan 1986; Hendon and Liebmann 1990; Mo 2000; Higgins and Shi 2001; Jones and Carvalho 2002; Wheeler and Hendon 2004, hereafter WH04; and others). Furthermore, westerly wind events related to the MJO significantly modify the thermocline structure in the equatorial Pacific Ocean via downwelling oceanic Kelvin waves, and the wave activity affects the overall intensity of El Niño episodes (McPhaden 1999, 2004; Kessler and Kleeman 2000; Zhang and Gottschalck 2002; Seo and Xue 2005). Also, the MJO has been known to modulate tropical cyclone activity in the Indian, Pacific, and Atlantic Oceans and the Gulf of Mexico (e.g., Maloney and Hartmann 2000; Mo 2000; Higgins and Shi 2001), and the intensity of both the mean South Atlantic convergence zone around Brazilian coast and South Pacific convergence zone to the east of Australia (e.g., Kousky and Kayano 1994; Matthews et al. 1996; Carvalho et al. 2004).

It is now widely appreciated that sea surface temperature (SST) variation and air–sea coupling are important processes for the development and maintenance of observed MJO characteristics. Krishnamurti et al. (1988) present evidence of SST fluctuations in relation to the MJO over the tropical warm pool and Wang and Xie (1998) show the importance of the ocean mixed layer thermodynamics in MJO dynamics. Many other analyses provide significant evidence of the role of the coupled air–sea interaction on the MJO (Zhang 1996; Shinoda et al. 1998; Woolnough et al. 2000; Hsu and Weng 2001; Kemball-Cook and Wang 2001, among others). Most previous modeling studies also support the notion that interactive air–sea coupling improves the MJO simulation (e.g., Flatau et al. 1997; Wang and Xie 1998; Waliser et al. 1999; Kemball-Cook et al. 2002; Fu et al. 2003). Especially, a general circulation model (GCM) simulation with prognostic SST anomalies by Waliser et al. (1999) confirms that the frictional wave–conditional instability of the second kind (CISK) process is operative on the equator as the maintenance and propagation mechanisms of the MJO.

Compared to the worldwide influence of the MJO on local weather and climate, only limited success has been realized in skillfully forecasting the oscillation evolution, especially using GCMs. Previous studies on the MJO forecast performance in dynamical extended-range forecast (DERF) experiments conducted with the National Centers for Environmental Prediction (NCEP) operational GCM (Global Forecast System, hereafter GFS) (Jones et al. 2000; Seo et al. 2005) revealed that the useful forecast skill of the MJO extends out to only nine days for the winter season. This is well below the potential predictability estimated by twin predictability experiments using the National Aeronautics and Space Administration (NASA) Goddard Laboratory for Atmospheres GCM in Waliser et al. (2003). They show a theoretically possible MJO forecast limit extending out to ~30 days for 200-hPa velocity potential and out to ~15 days for rainfall anomalies. Recently, a new atmosphere–ocean coupled Climate Forecast System (CFS) model has been developed and implemented at NCEP (Wang et al. 2005; Saha et al. 2006). The availability of daily data from the CFS for both operational forecast and hindcast provides a unique opportunity to assess the MJO prediction skill. Evaluation of the coupled dynamical model and the effect of interactive air–sea coupling are now possible. Moreover, although the current NCEP CFS uses a 2003 version of the GFS as the atmospheric component and has been frozen since 2004 for NCEP seasonal forecast, the NCEP GFS model, which is for operational medium-range forecast, is upgraded frequently (about twice per year); therefore, it is interesting to investigate to what extent GFS upgrades improve the MJO forecast. These estimates of the ability of MJO forecasting are especially important because the MJO temporal scale bridges the gap between synoptic weather forecasting and seasonal climate forecasting, and the information on the MJO-related weather and climate can benefit global regions with a high population density.

MJO prediction beyond lead times that the dynamical forecast models provide is routinely extended through statistical prediction techniques. First, Waliser et al. (1999) developed a statistical model based on singular value decomposition to 30–70-day bandpassed outgoing longwave radiation (OLR) anomalies. The model predicts future OLR anomalies using previous and present pentads of OLR anomalies as predictors. The prediction skill of their model extends out to 5–20 days over a large portion of the Eastern Hemisphere. Lo and Hendon (2000, hereafter LH00) developed a multiple linear regression model using least squares estimation to the spatially filtered daily OLR and streamfunction anomalies. The first two principal components (PCs) of OLR and the first three PCs of streamfunction from empirical orthogonal functions (EOF) analysis are chosen to predict OLR anomalies. This model provides useful skill out to a lead time of 15 days. Another empirical technique by Wheeler and Weickmann (2001) used Fourier filtering to predict the MJO and coherent synoptic tropical variability. It involves a separate forward and backward fast Fourier transform pair performed on OLR anomalies at each latitude. Their model extends the useful prediction skill of the MJO out to 15–20 days. Also, Jones et al. (2004) developed a statistical prediction model based on a lagged linear regression of the first five PCs from a combined EOF analysis of filtered

pentad OLR and 200- and 850-hPa zonal wind anomalies (U200 and U850 for short). Their model produces a prediction skill in the range of three to five pentads. Note that the use of bandpass-filtered anomalies in the construction of the statistical prediction schemes in Waliser et al. (1999) and Jones et al. (2004) provides statistical potential predictability of the MJO. Recently, Maharaj and Wheeler (2005) developed vector autoregressive (AR) models (VARs) using the MJO index time series of WH04 and demonstrated a skillful forecast out to ~14–17 days. Overall, the prediction skills of the statistical models estimated for real-time application are generally accurate for a period in the order of 15–20 days. Because of the differences in the treatment of the input and output data, and in the period tested, a direct comparison among the statistical models, and between statistical models and dynamical models, is difficult. A rigorous comparison of different forecast tools is desirable for an optimal MJO forecast.

The previous method used by Jones et al. (2000) and Seo et al. (2005) to extract the intraseasonal signal from the GFS DERF run is based on padding of observed data at the beginning of the dynamical model forecast data. The expanded data are then subject to a conventional bandpass filtering. This treatment tends to inflate the forecast skill as a result of the propagation of observed information into the forecast data. Additionally, given that operational dynamical forecast models produce outputs of relatively short duration (typically shorter than the MJO period), it is necessary to apply an efficient method that can extract the MJO signal without resorting to filtering in the frequency space. Therefore, the empirical methods developed by LH00 and WH04 are employed for the assessment of skill. They have calculated an all-season MJO index for real-time monitoring by projecting daily observed data, with annual cycle and interannual variability eliminated, onto a leading pair of EOFs of the combined fields of equatorially averaged OLR, and 850- and 200-hPa zonal wind anomalies. This method has been proven to be very effective for the real-time extraction of the MJO-related variability, and here we apply this method to the outputs of NCEP's global coupled and uncoupled models. In addition, there arises a need to compare the MJO prediction skills from the GCM forecast outputs with those from statistical prediction schemes in a consistent manner. This is possible if statistical prediction schemes are developed and applied in the space of coefficient or PC time series, which are derived by the above-mentioned real-time signal extraction method.

In this study, the MJO dynamic predictability is assessed based on the real-time MJO PC indices from the observed data and forecast outputs of NCEP's atmosphere-only and atmosphere–ocean coupled models. In addition, various empirically derived prediction models, such as lagged multiple linear regression and autoregressive models, are developed and compared with the dynamical predictions. This skill assessment in GCMs and statistical forecast models serves as a benchmark for evaluating the MJO forecast skill and the inclusion of the forecast skill from several other statistical and dynamical models is always possible, thus facilitating a straightforward performance comparison between the applied models. Next are three questions will be addressed.

1) To what extent does the MJO forecast benefit from the inclusion of the air–sea interaction?
2) Does the improvement in the model physics and initial conditions lead to better MJO forecast?
3) How do the statistical tools compare with each other and how do they compare with the dynamical models?

2. The models and simulations

a. Datasets

To capture the convectively coupled, large-scale circulation signal associated with the MJO, OLR, as a proxy for deep convection, and zonal winds at the upper and lower levels (200 and 850 hPa) are used. OLR is derived from the Advanced Very High Resolution Radiometer on board the NOAA polar-orbiting satellites (Liebmann and Smith 1996). The gridded daily OLR data are available at NCEP in near-real time. For the zonal winds, the NCEP/Department of Energy (DOE) Global Reanalysis 2 (GR2; Kanamitsu et al. 2002) is used. Both datasets are on a 2.5×2.5 longitude–latitude grid. Using the daily data from 1982 to 2004, the EOFs of the combined fields of the three variables are calculated.

b. The NCEP model forecast

The performance of the NCEP's CFS model prediction for the MJO is assessed. The atmospheric component of the coupled CFS is the 2003 version of the NCEP GFS (interchangeably referred to as GFS03). It adopts a triangular truncation of 62 spectral waves (T62) in the horizontal and 64 sigma layers in the vertical. The oceanic component is the Geophysical Fluid Dynamics Laboratory Modular Ocean Model, version 3 (MOM3; Pacanowski and Griffies 1998). The spatial domain for MOM3 in CFS is quasi global, extending from 74°S to 64°N. The zonal resolution is 1° and the meridional resolution is 1/3° between 10°S and 10°N, linearly increasing to 1° poleward of 30°S and 30°N. There are 40 layers in the vertical with 27 layers in the

upper 400 m. The atmospheric and oceanic components are coupled daily. Sea ice extent is prescribed from the observed climatology. An upgraded version of the simplified Arakawa–Schubert scheme is used for cumulus convection parameterization. More details of the CFS model can be found in Saha et al. (2006) and Wang et al. (2005). Forecast initial conditions are provided from the NCEP global ocean data assimilation system (GODAS) for the ocean and from GR2 for the atmosphere.

There are two types of CFS forecast: retrospective (or hindcast) and real time. The CFS hindcast was made for the period from 1982 to 2004. For each starting month, the CFS hindcast is initialized from 15 different dates: days 1–3, 9–13, 19–23, and the last two days of the month. To calculate the seasonal cycle for each lead time and initial date, the cubic spline method is used for filling the forecast gaps. For each forecast, only the first 45 days are used for this study. Hindcast data from uncoupled atmospheric GFS are not available for 1982–2004. Therefore, only CFS hindcast skill will be compared to the skill from the statistical forecast models.

The CFS was implemented in August 2004 for real-time forecast. One forecast member was produced from August to December 2004. Starting January 2005, two forecast members have been produced. The two members are initialized with identical GODAS initial conditions for the ocean. For the atmosphere, both members use GR2 0000 UTC initial conditions, with small perturbations added to one member. We use CFS daily forecast output from January 2005 to February 2006. Furthermore, to examine the effect of interactive air–sea coupling on the MJO forecast skill, the uncoupled offline 45-day GFS forecast has been independently performed since 2005. This offline GFS forecast uses exactly the same initial conditions for the two members as the operational CFS model forecast.

The NCEP operational GFS run produces a 15-day forecast dataset each day. The daily output is a 20-member ensemble mean. This operational GFS model has undergone substantial changes since 2003 and is different from the above offline GFS model, which is the atmospheric part of the coupled CFS model. For example, since 31 May 2005, the resolution of the model has been increased from T254L64 (to 84-h integration), T170L42 (to 180 h), and T126L28 (to 15 days) to T382L64 (to 180-h integration) and T190L64 (to 15 days). There have also been a number of upgrades of physics to the operational GFS [a more detailed list of changes is available online at http://www.emc.ncep.noaa.gov/gmb/STATS/html/model_changes.html]. Therefore, we do not intend to evaluate the effects between different GFS model versions but rather the overall performance of the current operational global model.

c. Methods of analysis

The seasonal cycle, defined as the time mean and the first three harmonics of the annual cycle, is removed in real time at each grid point. For the observation, a cross-validated form of the seasonal cycle is prepared using 22 yr of data (with one year taken out from the 23-yr data). For the forecast data, the seasonal cycle for each forecast day and lead time are calculated to remove model bias. For the seasonal cycle of the offline GFS model forecast, the independent hindcast integration was performed from 1999 to 2004. The integration length of this independent hindcast is 45 days. In the case of the operational GFS model forecast, the frequent model updates do not allow for the production of a hindcast dataset. Instead, the seasonal cycle from the above miniclimatology by the offline GFS run will be used as an ad-hoc seasonal cycle. The data periods for the seasonal cycle and skill evaluation of hindcast and/or forecast in observations and dynamical and statistical models are summarized in Table 1.

Removal of the El Niño–Southern Oscillation (ENSO) variability follows the methods proposed by LH00 and WH04. Because ENSO anomalies in convection and dynamical fields resemble one dominant phase of the MJO, this removal is of critical importance. For example, enhanced convection over the Maritime Continent and western Pacific, which has a strong projection to one of the leading EOF modes for the intraseasonally band-passed OLR anomaly, occurs during a typical La Niña event. Without this removal, strong ENSO periods keep producing the strong MJO phase. The ENSO signal is identified from EOF analysis of daily SST anomalies in the tropical Pacific domain (30°S–30°N, 120°E–80°W). Daily SSTs are produced by linear interpolation of the weekly analysis of the optimally interpolated SST (OISST) of Reynolds et al. (2002). The leading two EOFs and both PCs capture interannual variability especially associated with ENSO (not shown). The first EOF (which explains 35% of the total daily variance) captures ENSO-related SST variability and the second EOF (which explains 10% of the daily variance) represents the interesting difference between the strong cold and warm ENSO events. Since this latter mode has strong positive loadings during both El Niño and La Niña events, a cold event is considered to be more concentrated in the central Pacific Ocean, whereas a warm event has large positive SST anomalies extending to the eastern Pacific (see also LH00). The variability that is linearly related to this interannual variability is calculated for each variable and is subtracted from seasonal cycle–removed anomalies in real time. The spatial distribution of the OLR anomaly that is linearly

TABLE 1. Data periods for seasonal cycle and skill evaluation for hindcast and/or forecast in observations and dynamical and statistical models.

Observations and models	Seasonal cycle	Skill evaluation period for hindcast and/or forecast
Observations	A leave-one-out approach for 1982–2005	1995–2004 (hindcast) 2005/06 (forecast)
Hindcast CFS	1982–94	1995–2004 (hindcast)
Offline GFS	1999–2004	2005/06 (forecast)
Operational GFS	Seasonal cycle of offline GFS	2005/06 (forecast)
Operational CFS	1982–94 (hindcast CFS)	2005/06 (forecast)
Statistical models	1982–94 (observations)	1995–2004 (hindcast) 2005/06 (forecast)

associated with the ENSO variability is determined by projecting OLR, U200, and U850 anomalies onto PC1 and PC2 of SST EOF modes for each month. For the daily use, the resulting monthly fields are converted to the daily maps. The details of the preparation of the linear component associated with the interannual variability are explained in WH04. An additional moving average or spatial filtering used in LH00 and WH04 has not been employed in this work.

After application of the above-mentioned methods for removing the longer time-scale variability, the MJO-dominant signal can be extracted without resorting to bandpass filtering in the time domain. Following WH04, EOF analysis of the combined fields of OLR and 850- and 200-hPa zonal winds averaged over (15°S, 15°N) is performed for the 1982–2004 period to identify the dominant MJO structure. Prior to input into the EOF analysis, each variable is normalized by its globally averaged variance, so each variable retains the same amount of weighting in the calculation of the variance of the combined fields. The two leading EOF modes are shown in Fig. 1. The EOF1 of the observation (Fig. 1a) is characterized by a strong convective heat source over the Maritime Continent and the western Pacific (100°–160°E), and the consistent convergent flow in the lower troposphere and divergent flow in the upper troposphere, reminiscent of a Gill-type response. In the EOF2 (Fig. 1b), strong convection is located over the Indian Ocean (60°–100°E). The corresponding PCs (not shown) are highly correlated with a certain lag, such that PC1 leads PC2 by a quarter cycle (i.e., ~10–12 days). Taken together, this describes the large-scale, eastward-propagating, convection–circulation signal. The first two PC time series can be represented as successive points in the (PC1, PC2) phase space, with counterclockwise movement of the center of the intraseasonal signals illustrating the eastward propagation. It should be noted that the PCs occasionally exhibit somewhat wild day-to-day variations and that these fluctuations are systematically associated with convectively coupled Kelvin waves and equatorial Rossby (ER) waves (Roundy et al. 2009). The ER waves are related to abrupt changes in the direction of trajectories in the phase space, while the Kelvin waves are associated with rapid progression of trajectories. However, the MJO and the convectively coupled Kelvin wave share some characteristics. This can be seen from the connected power spectra between the MJO and the Kelvin wave (Fig. 3 of Wheeler and Kiladis 1999; Fig. 1 of Roundy et al. 2009). It is understood that the nominal MJO propagation speed is ~5–8 m s^{-1} over the Indian Ocean and the western Pacific, but it is ~10–15 m s^{-1} over the western hemisphere (e.g., Hendon and Salby 1994, 1996). The latter is usually the result of the MJO dynamical component, since MJO convection vanishes over the eastern Pacific. This propagation feature also appears in the equatorial Kelvin wave and the MJO sometimes includes some portion of the Kelvin wave. If this broad definition of the MJO is considered, then the PCs resulting from the above calculations mostly represent the MJO component. However, the time series still contain convectively coupled ER and Kelvin wave components not projected on this broadly defined MJO. The MJO convection–circulation regime generally divides the global tropics into eight different phases. The composite OLR and U850 fields for the eight phases for the winter and summer seasons show that similar patterns appeared in WH04 (not shown).

Again, the advantage of this method is that it can be applied to data with any length as well as in real time. Since operational forecast data are short compared to the MJO time scale, the above procedure is applied to produce the MJO-related component in real time.

3. Empirical forecast models

Statistical forecast models are also developed using the 1982–2004 data, and the first two PCs are used for the construction of the models. Daily PC1 and PC2 are converted to pentad points for simplicity. To develop the statistical models, the first 13 yr of sample data are used as development or dependent data. The last 10-yr data are used as validation or independent data. The statistical models are constructed in phase space rather

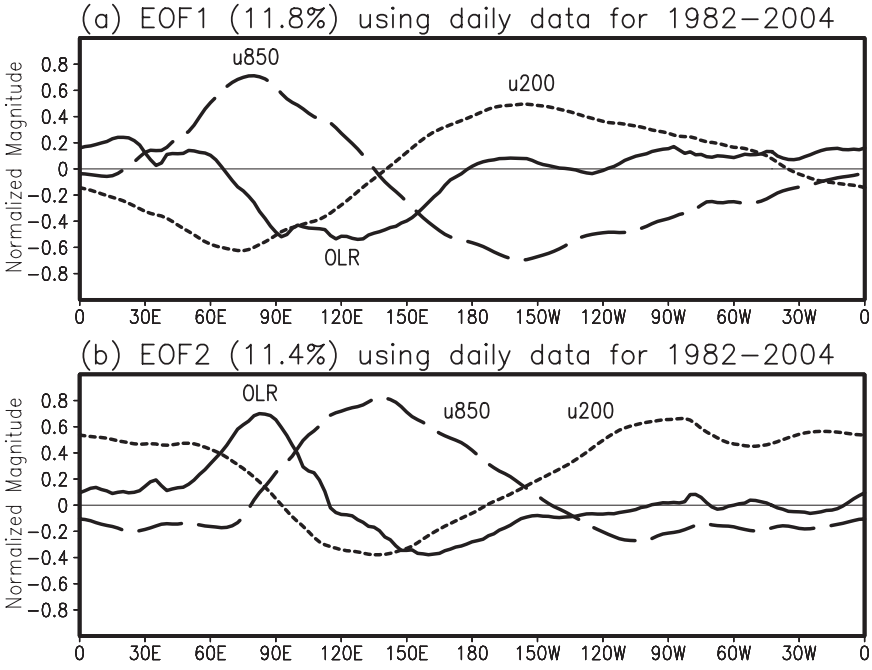

FIG. 1. (a) EOF1 and (b) EOF2 spatial structures of the combined analysis of interannual variability–removed OLR, U850, and U200. The variables are averaged over (15°S, 15°N). All variables are normalized by the averaged value of global variance (15.0 W m^{-2} for OLR, 1.9 m s^{-1} for U850, and 4.9 m s^{-1} for U200).

than physical space to reduce the degree of freedom of the field variables.

The first model is a lagged multiple linear regression model (which is referred to as PCRLAG). This prediction scheme is based on the previous values of the first two PCs and takes the following form:

$$\mathrm{PC}_k(t+h) = \sum_{j=1}^{J}\sum_{i=1}^{I=2} C_{kij}(h)\mathrm{PC}_i(t-j+1) + \varepsilon_{t+h}, \quad (1)$$

where i and k are the PC indices and the regression coefficients of kth PC, $C_{kij}(h)$ are a function of each lead time (or forecast horizon) h, PC_i, and lags j. The regression coefficients are determined by least squares estimation. Here, ε_{t+h} are random errors and assumed to be normally distributed. Since PCs are orthogonal to each other, the strong interrelationships inherent in the predictors do not exist, which thereby guarantees a unique estimate of the regression coefficients. Figure 2a shows the forecast skill of the PC1 model for different lags as computed from the training data. It is evident that the forecast skill significantly improves when the applied lags are greater than one pentad but the use of more than five pentads does not improve skill. Therefore, five pentad lags ($J = 5$) are chosen here, which is consistent with the lagged multiple linear regression model used in Jones et al. (2004). The correlation skill of the PC2 phase according to the employed lags exhibits similar behavior to the PC1 model and is not shown here. The simplest model for constructing a multiple linear regression scheme is to use only the latest pentad. From (1), this model is the case when $J = 1$ and denoted as PCR.

Another statistical forecast model is to fit the time series using an AR model. An AR of order J can be written as

$$PC_k(t+1) = \sum_{j=1}^{J} C_{jk} PC_k(t-j+1) + \varepsilon_{t+1}, \quad (2)$$

where C_{jk} are the coefficients of the AR determined by the Yule–Walker relations for lag j and PC_k, and ε_{t+h} are random components. Therefore, the first pentad forecast of one PC time series is determined by the previous J pentad points of its own PC, and the second pentad forecast is calculated by the previous $J - 1$ pentad PCs and the forecasted PC, and so on. Here the best order of the AR is determined objectively by the criterion of autoregressive transfer function (Newton 1988) and the selected order is five ($J = 5$), as in Jones et al. (2004).

The fourth forecast scheme is based on the extrapolation of the eastward propagation speed in the WH04's phase diagram. In this empirical phase propagation (EPP)

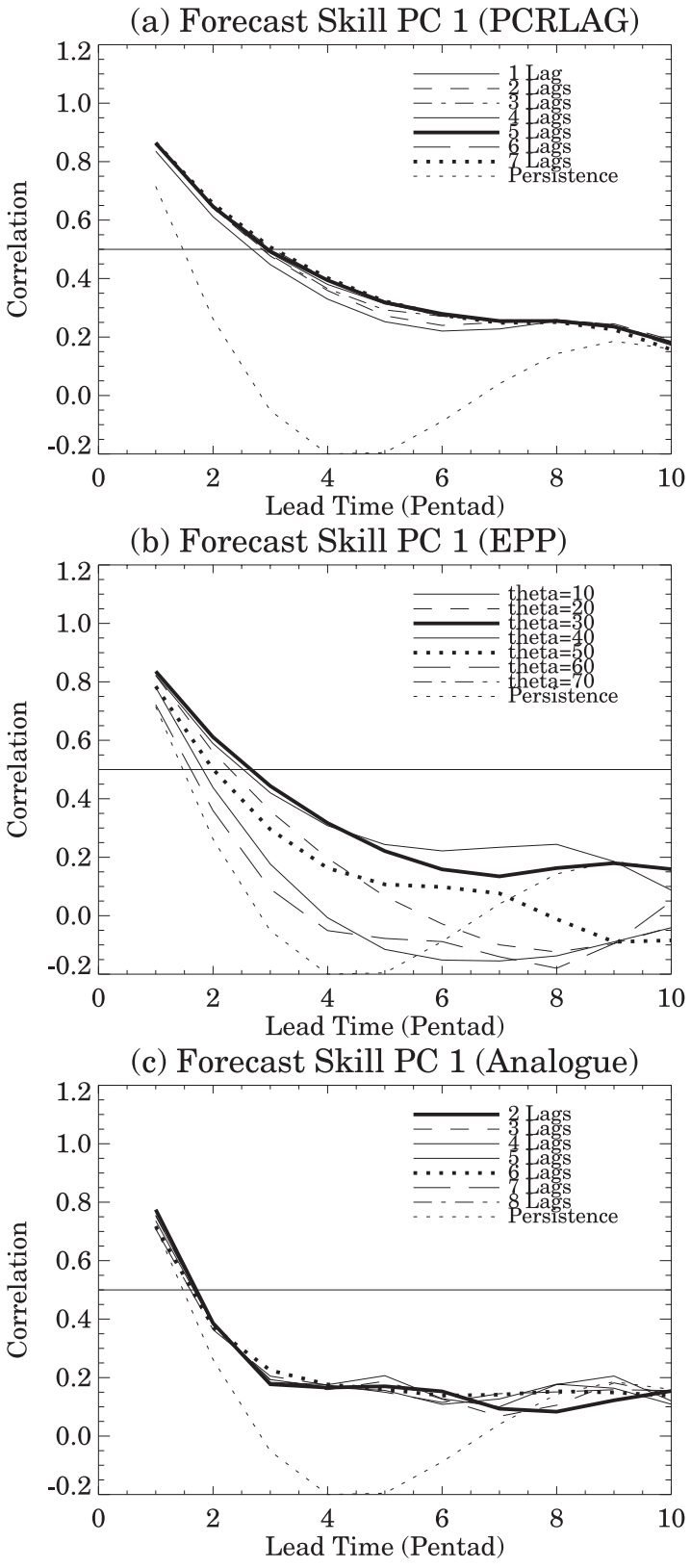

FIG. 2. Sensitivity test for forecast skill of PC1 for (a) PCRLAG, (b) EPP, and (c) ANALOG. In (b), theta means $d\theta$(° pentad^{-1}) in (3).

model, the propagation speed is expressed as the longitudinal translation degree per pentad in an anticlockwise sense in the phase diagram, and the amplitude is assumed to be fixed as its latest observed value. Then, the prediction scheme takes the following form:

$$\theta(t+1) = \theta(t) + d\theta,$$

$$\theta(t) = \tan^{-1}[\mathrm{PC}_2(t)/\mathrm{PC}_1(t)],$$

$$\mathrm{PC}_1(t+1) = \sqrt{\mathrm{PC}_1^2(t) + \mathrm{PC}_2^2(t)}\cos[\theta(t+1)], \quad \text{and}$$

$$\mathrm{PC}_2(t+1) = \sqrt{\mathrm{PC}_1^2(t) + \mathrm{PC}_2^2(t)}\sin[\theta(t+1)], \qquad (3)$$

where $d\theta$ is determined using the training data. Figure 2b shows the correlation skill of PC1 for some propagation speeds in term of longitudinal degrees. From this, 10°–20° is too slow eastward propagation but 50°–70° is too fast eastward propagation. The propagation speed of 30° pentad^{-1}, which corresponds to ~7 m s^{-1}, provides the highest skill score with the most useful skill out to ~3 pentads. The same applies to the PC2 (not shown). This EPP is similar to an empirical mode propagation method applied in physical space by Van den Dool (2007).

The final empirical method is a natural analog method (referred to as ANALOG), which identifies prior states that are close to the current state. Assuming that the current state evolves in a similar way to the identified analogs, future values can be estimated as an ensemble mean evolution of individual analogs. Here the nearest analogs are found by the root-mean-square difference between the current state and the identified analog in the PC space. Figure 2c shows the forecast skill of PC1 for different numbers of the latest pentad lag (two to nine lags) that are used in the computation of the RMS difference. In this case, the first 40 closest analogs are selected. The forecast skill is fewer than two pentads for the entire range of lags and the use of just two previous pentads results in the best skill. The results are not affected by the number of the selected analogs.

Using the above empirical forecast models, a statistical ensemble mean forecast scheme (ENS) is also constructed. The weighting coefficients of the individual components are derived by performing multiple linear regressions against the observation. The coefficients are, of course, a function of lags and PC modes.

4. Empirical and dynamical forecast skills using the 1982–2004 data

Figure 3 shows the correlation and RMS error skill of PC1 and PC2 as a function of forecast lead time during the validation period (1995–2004) for the coupled CFS hindcast and empirical forecasts. A useful skill is defined as a correlation exceeding 0.5 (horizontal line). The forecast skill ranges from two to three pentads for both PC1 and PC2. The best empirical model is PCRLAG, with a useful skill extending to three pentads for both PCs. EPP and PCR, which exhibit almost the same variation of correlation skill, produce slightly lower skill than PCRLAG. AR and ANALOG show the lowest forecast skill—out to two pentads. Note that the source of skill in these empirical forecast schemes lies in both the autocorrelation of each PC and the lagged cross correlation between two PCs. Therefore, PCRLAG and PCR predict better than AR and ANALOG, which only rely on the autocorrelation of their own PC. Since correlation skill does not provide information on forecast amplitude error (Hoffman et al. 1995), RMS error should be separately evaluated. The behavior of the RMS error is virtually consistent with the variation of the above correlation skill. The PCRLAG method exhibits the lowest RMS error for all lead times. The normalized RMS error increases with forecast lead time at the beginning and saturates after five pentads. The forecast skill, using the whole CFS hindcast period from 1982 to 2004, shows almost the same results as those calculated for the validation period (not shown). The forecast skill of ENS is compared with the best statistical model, PCRLAG, in Fig. 4. Ensemble members are the above empirical methods except for ANALOG, which produces the worst skill. It shows that ENS has little improvement over PCRLAG for pentad lead times from one to four. For larger lead times, a slight but not significant improvement appears.

Interestingly, the PC1 phase shows a forecast skill of two pentads but the PC2 phase has a useful skill up to three pentads. The forecast skill of PC2 in the CFS hindcast is nearly the same as that from the best empirical model, indicating that the MJO dynamical forecast has some usefulness. The primary reason for this difference between PC1 and PC2 may be due to a propagation barrier across which the intraseasonal signal is unable to move, since previous analyses on the long-term simulation of the coupled CFS model (Seo et al. 2007) and DERF run with the GFS model (Seo et al. 2005) suggest the existence of a barrier over the Maritime Continent and western Pacific. Figure 5 illustrates this property. Figure 5a is a composite plot of the U850 averaged between 15°S and 15°N, and Fig. 5b is a composite plot of forecast U850 for the corresponding phase. Again, the extreme phases have been determined by the normalized PCs of the combined EOF analysis on OLR and upper- and lower-level circulations. The observed zonal wind anomalies propagate eastward.

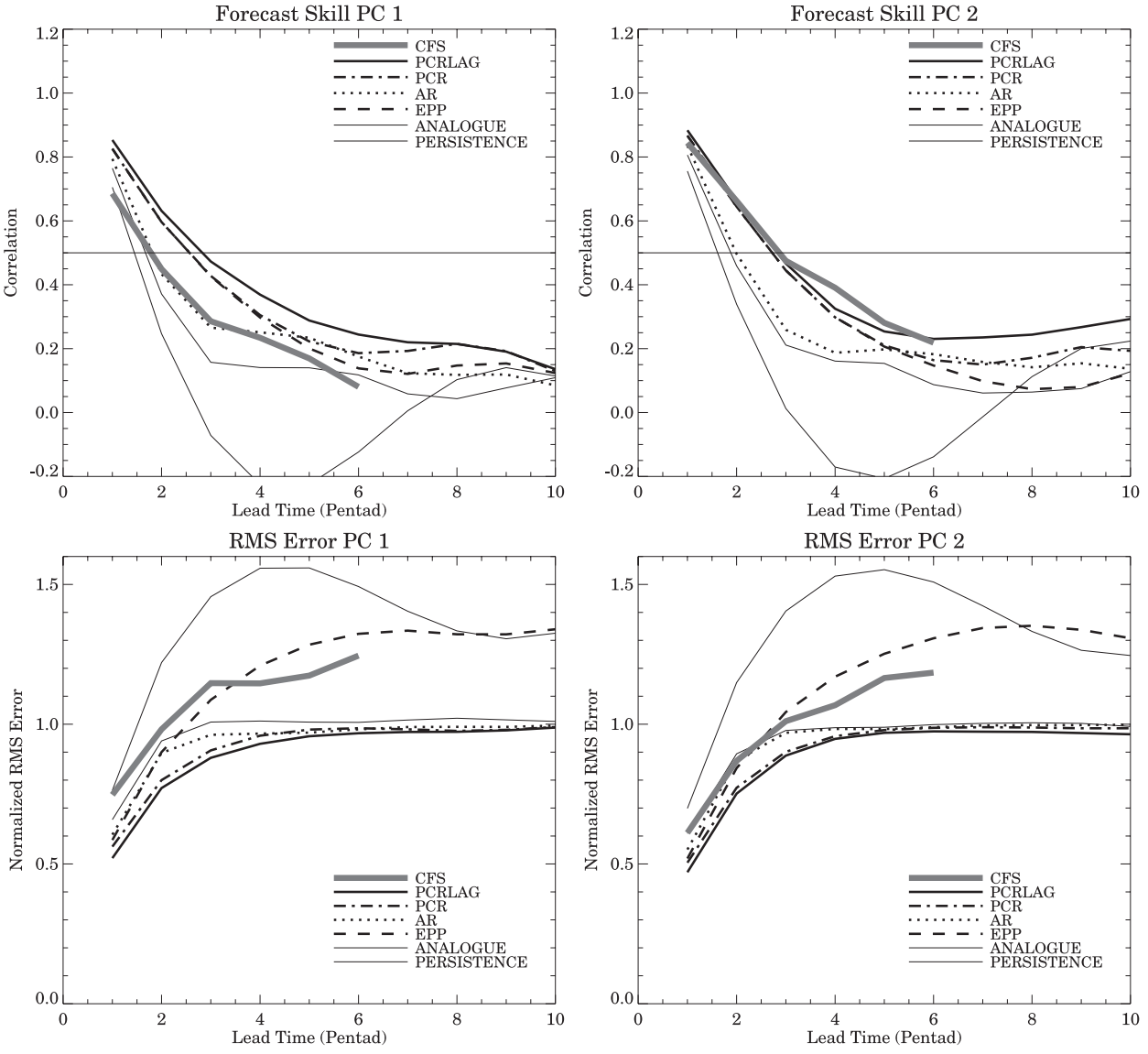

FIG. 3. (top) Correlation skill and (bottom) normalized RMS error as a function of forecast time (pentad) for (left) PC1 and (right) PC2. The calculation is based on the 10-yr (1995–2004) validation data.

The propagation in the observation is faster over the western Pacific than over the Indian Ocean, which is consistent with our understanding. In the forecast, enhanced convection initially located over the Maritime Continent (i.e., PC1 + phase) is not able to cross this region. When enhanced convection is originally situated over the Indian Ocean (i.e., PC2 − phase), the MJO signal can propagate eastward until it reaches the barrier, as shown in the observation, although the propagation speed in the hindcast is less than in the observations.

It is interesting to examine the dependence of forecast skill on the initial forcing magnitude in the statistical and dynamical forecasts. Here the MJO initial forcing magnitude is represented by the PC amplitudes. Figures 6 and 7 show the forecast skill as a function of the PC amplitude for the best empirical model (i.e., PCRLAG) and the CFS hindcast, respectively. It is evident that the skill in both the PCRLAG and CFS hindcast increases with increasing initial MJO signal strength for lead times from pentad 1 to pentad 2, which is consistent with the previous findings. However, for the PCRLAG PC1 case (Fig. 6a) with an initial amplitude greater than 2.0, the skill is lower than the case with the initial strength of 1.5–2.0. This may be related to the fact that the statistical model is a damped oscillatory system and thus the trajectory of the MJO centers predicted from

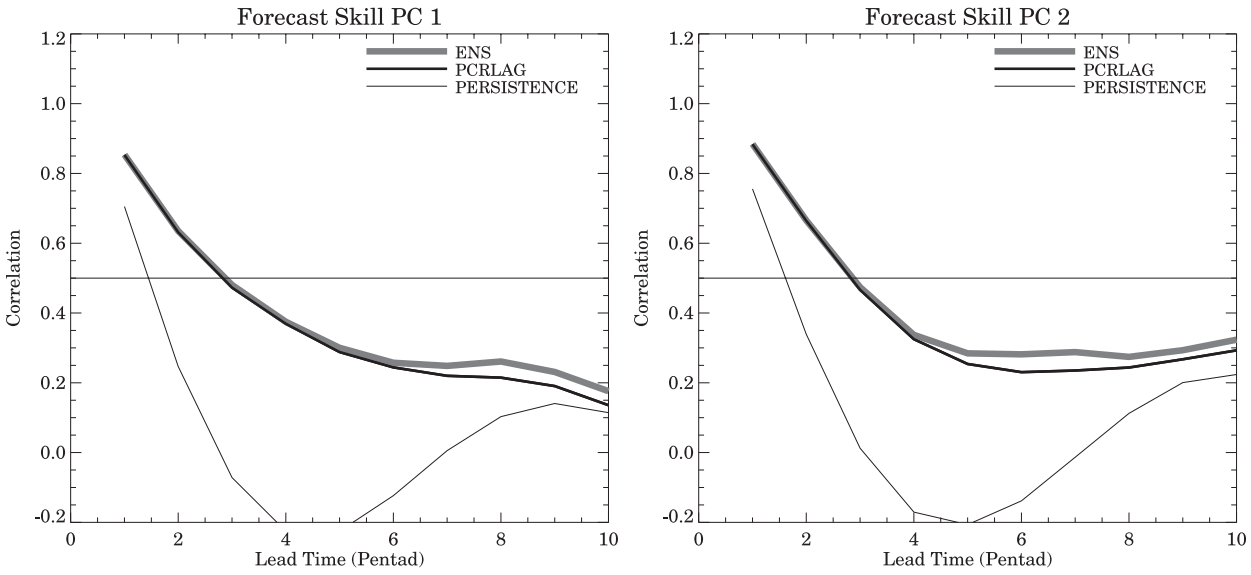

FIG. 4. Correlation skill of ENS and PCRLAG as a function of forecast time (pentad) for (left) PC1 and (right) PC2. The calculation is based on the 10-yr (1995–2004) validation data.

the initially strong MJO amplitude tends to quickly converge into the origin. The relationship between the initial amplitude and the forecast skill for the pentad 3 forecast is not as clear as that for pentads 1 and 2, especially for the CFS hindcast data. So in general, for up to forecast pentad 2, the forecast skill increases as the initial MJO forcing increases. Finally, a comparison of PC1 and PC2 in Figs. 6 and 7 shows that the PC2 cases with an initial amplitude greater than 2.0 result in a higher overall skill than that of the PC1 cases. This suggests that a more skillful forecast for the PC2 phase compared to the PC1 phase, as seen in Fig. 3, may be attributed to a higher skill associated with the stronger initial amplitude in the PC2 phase.

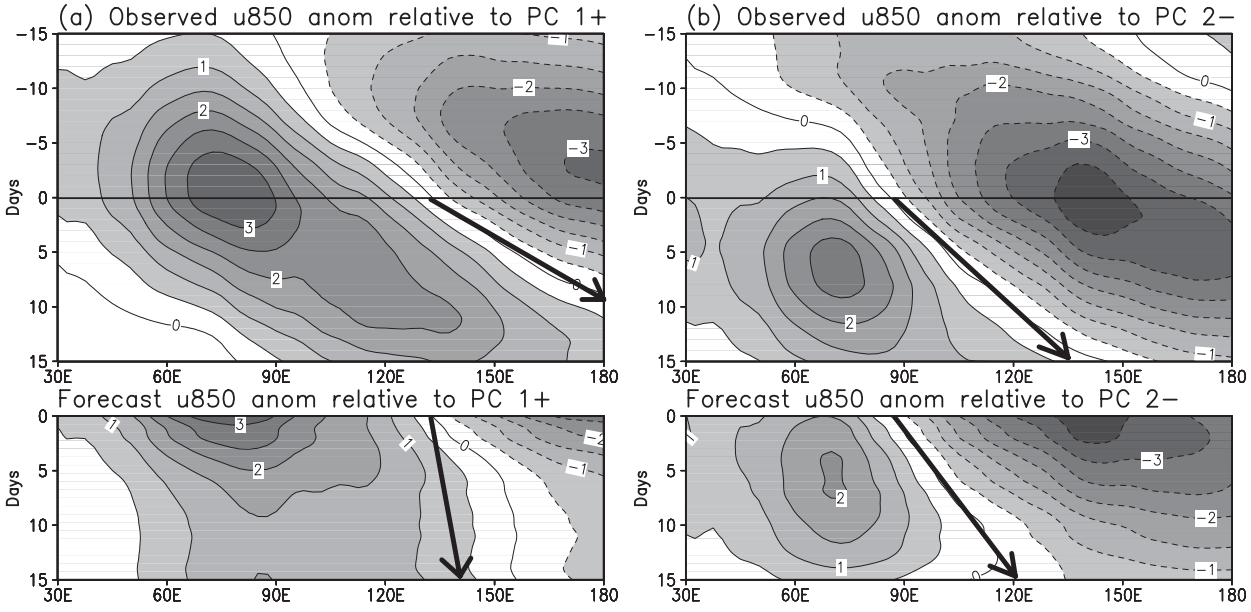

FIG. 5. Time evolution of U850 averaged between 15°N and 15°S for enhanced initial condition. (a) +PC1 and (b) −PC2. The top (bottom) panel is a composite plot of the analysis (forecast, respectively) U850. The contour interval is 0.5 m s^{-1}. The thick arrow denotes the propagation of the MJO convection.

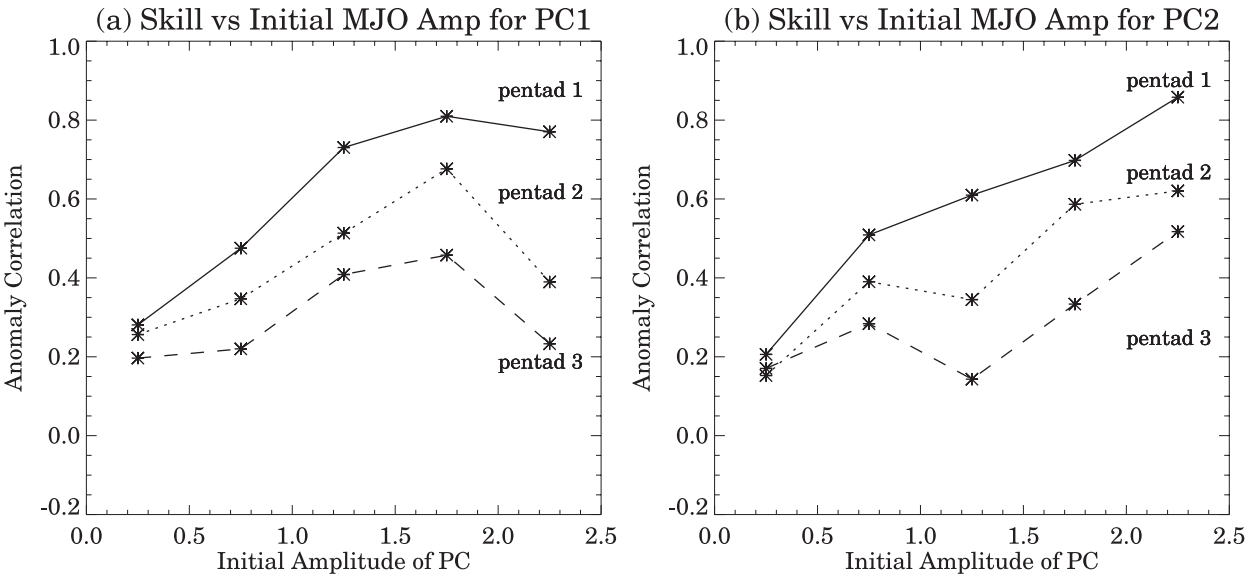

FIG. 6. Correlation skill as a function of initial amplitude of (a) PC1 and (b) PC2 for PCRLAG. The band of initial amplitudes is 0.5 and the correlation is marked at the midpoint of each band.

5. Real-time evaluation of empirical and dynamical forecast skills

At NCEP, daily CFS forecasts have become operational since August 2004. As the OISST analysis is updated weekly, the CFS forecast runs retroactively with a 7-day delay. An effort to run this in real time is underway. However, for real-time dynamical forecast, operational GFS run output can be used, and currently the daily evaluation is performed in an automated mode.

Forecast skill from the CFS model (referred to as CFS03) and its atmospheric component GFS03 are calculated for the period from January 2005 to February 2006 (Fig. 8). Figure 8 also shows the daily real-time predictions from the two statistical models: PCRLAG and AR. These two models use 15 daily lags and an order of 15 for the PCRLAG and AR, respectively (see the appendix for the PCRLAG equations with explicit parameter values). The forecast performance of another statistical model using VAR developed by Maharaj and

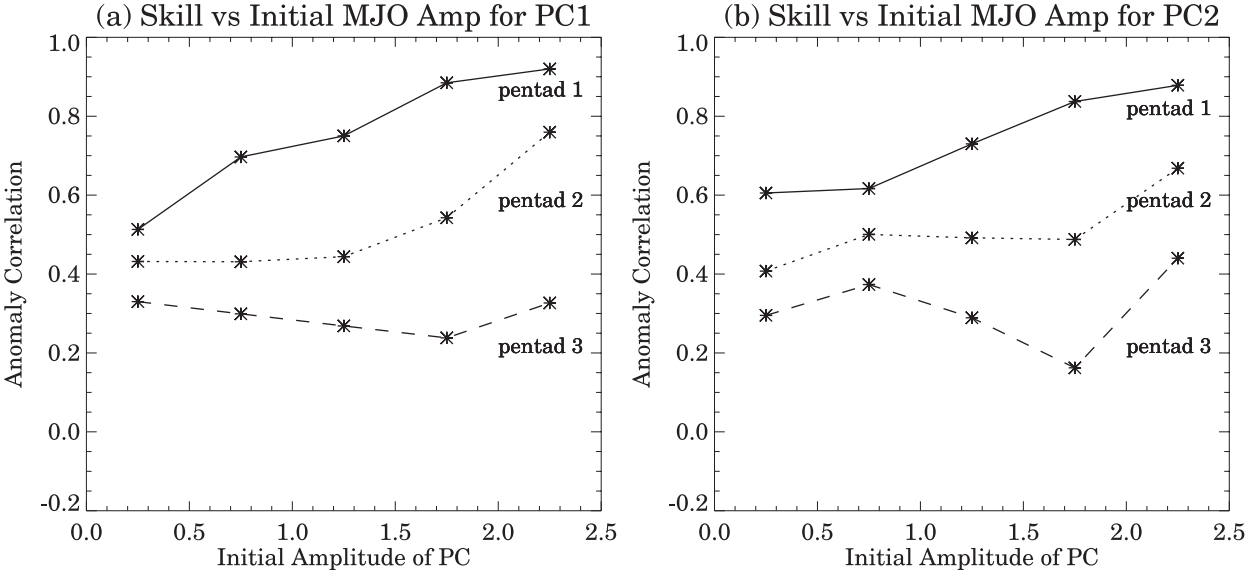

FIG. 7. Same as Fig. 6 but for CFS hindcast.

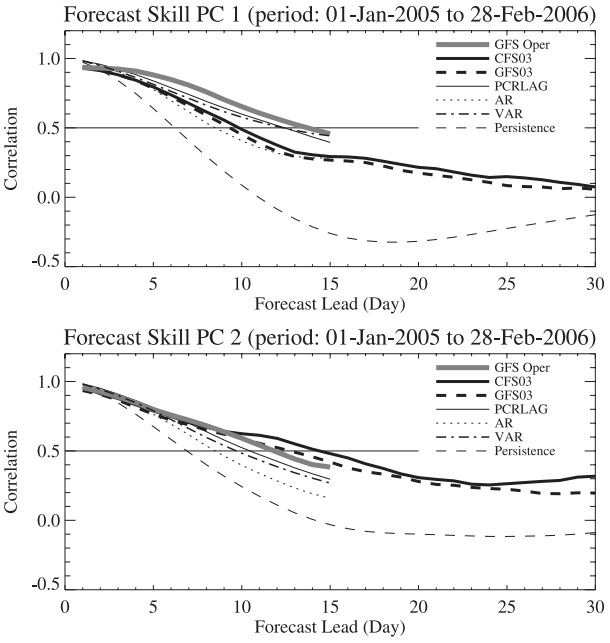

FIG. 8. Correlation skill of PC1 and PC2 as a function of forecast day for CFS03 (operational coupled model), GFS03 (offline atmospheric model), PCRLAG, AR, and VAR during 2005/06. The correlation skill of the operational GFS forecast is denoted as a thick gray line.

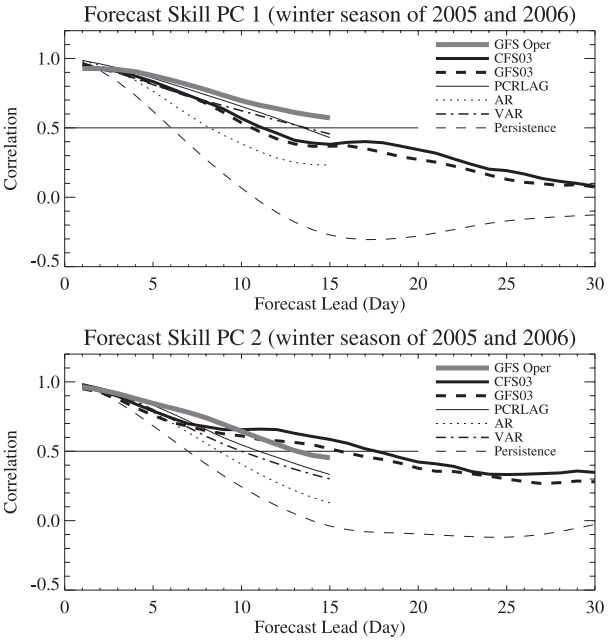

FIG. 9. Correlation skill of PC1 and PC2 as a function of forecast day for CFS03, GFS03, PCRLAG, AR, and VAR during the winter season for 2005/06. The correlation skill of the operational GFS forecast is denoted as a thick gray line.

Wheeler (2005) is also presented as the benchmark statistical model. This model uses the PC indexes originally computed in WH04 (which are almost the same as the PC time series of this work), and the first-order VAR model is found to be the most optimal for forecasting the indices. Since the VAR parameters for daily data are explicitly revealed in their paper, the straight calculation is possible for this period. In Fig. 8a for PC1, GFS03 shows useful skill out to ~10 days but PCRLAG gives a skillful forecast out to more than 13 days (Fig. 8a). Furthermore, CFS03 has better forecast skill than GFS03. For PC2, the skills from CFS03 and GFS03 are out to ~15 days, which is greater than the PC1 phase and is consistent with the hindcast analysis described in the previous section. Moreover, forecast skill from the dynamical models is better than PCRLAG and AR. This is related to the weak MJO activity during the 2005/06 winter season (see also Fig. 9), since forecast skill is proportional to the initial MJO magnitude, as in Fig. 6. Furthermore, we can see that the VAR model performs as well as PCRLAG, with only slightly less skill compared to the latter. Therefore, VAR and PCRLAG are considered good benchmark statistical models. The coupled model slightly beats the uncoupled model, indicating some improvement when interactive air–sea coupling is included, and this is the first result that shows the effect of the air–sea interaction on the MJO forecast in operational numerical models. Although the whole statistics show only a slight improvement, an inspection of some individual cases reveals a nonnegligible forecast improvement from the inclusion of the coupled air–sea interaction (figure not shown).

Figures 9 and 10 show the forecast skill as a function of forecast lead time during the winter and summer seasons, respectively. The skill during the winter season is larger by ~5 days than that during summer for the same PC. In addition, the increase of skill in PC2 (~4 days) is larger than that in PC1 (~2 days). Consequently, the skillful forecast for PC2 from CFS03 extends up to ~18 days in the winter, whereas for PC1 during summer it extends about one week. The PC1 skill of the operational GFS model forecast is greater than 15 days. The higher horizontal resolution and finer initial conditions might be important factors for this improvement, since the representation of the Maritime Continent region is improved. The enhanced representation of this region has led to a better MJO simulation in the study of Inness and Slingo (2006).

Currently, at the Climate Prediction Center (CPC) of NCEP, the real-time monitoring of the MJO forecasts is performed using the operational GFS forecast and a couple of statistical methods. For this, the phase diagram formed by PC1 and PC2, as in WH04, is used and the real-time update is made of the latest 40-day observed MJO evolution. Along with this observational

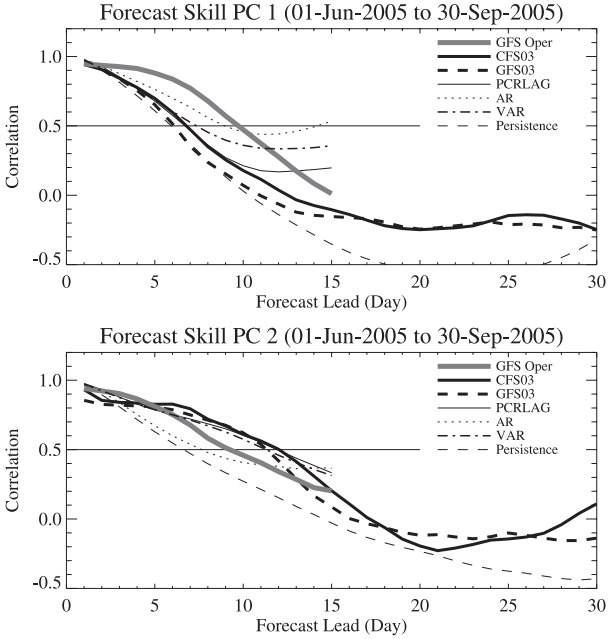

FIG. 10. Same as Fig. 8 but during the summer season of 2005.

analysis, real-time MJO forecasts are plotted. The statistical models PCRLAG and AR exhibit the anticlockwise rotation (i.e., eastward propagation), and they tend to converge into the origin as time passes because the prediction system by the statistical schemes corresponds to a damped oscillatory system. Usually, AR has a stronger damping than PCRLAG. The horizontal pattern with physical magnitude can be retrieved by multiplying the magnitude of PC1 and PC2 by their horizontal EOF patterns. The EOF patterns are obtained from composites of OLR, and U850 and U200 anomalies containing their meridional structure keyed to the time when the standardized PC1 or PC2 in Fig. 1 has one standard deviation variation. The predicted MJO horizontal patterns for different lead times are found on the CPC Web site. Another example of the operational use of the dynamical MJO forecast is the verification of the 15-day NCEP operational atmospheric and coupled forecasts (refer to CPC Web site). The real-time MJO monitoring, forecasts, and verification Web site is currently used to support the official operational CPC MJO weekly update and global tropics benefits/hazards assessments and to prepare for week 1 and week 2 weather and climate outlooks at NCEP.

6. Summary and discussion

This work examines the performance of MJO forecasts in the NCEP's fully coupled operational forecast model (CFS) and statistical prediction models. To avoid complications in extracting the MJO-related signal from the forecast data, a common filtering technique, dependent upon the convolution of a response function in the frequency domain, has not been used but rather the filtering method by WH04. The resulting indices show leading MJO signals, but these also contain day-to-day fluctuations systematically associated with convectively coupled Kelvin waves and ER waves (Roundy et al. 2009). However, this study employs a broad MJO definition, which includes some portion of the convectively coupled Kelvin wave activity at a higher frequency domain. The use of pentad averaging reduces the ER wave-related variability. This study assesses the effect of interactive air–sea coupling on MJO forecasts by comparing forecasts from the operational CFS model and its atmospheric component GFS model. By using this widely recognized MJO index, this assessment of the forecast skill in GCMs and statistical models serves as a benchmark for evaluating the MJO forecast skill. The inclusion of forecast skill from other statistical and dynamical models is always possible, and their skill comparison is feasible.

The coupled CFS model has useful skill out to 15 days, when the initial MJO convection is located over the Indian Ocean. The prediction skill of the CFS hindcast is nearly comparable to that from a lagged multiple linear regression model, which is the best empirical model among all the statistical forecast approaches. In contrast, the skill in the real-time forecast for the period of January 2005 to February 2006, using the lagged multiple linear regression model, is reduced to ~10–12 days, presumably as a result of the usage of daily data and thus an increased number of coefficients to be determined. The operational CFS forecast, for this period, however, is skillful out to ~15 days for the annual average and ~17 days for the winter months, thus indicating the greater usefulness of the coupled model forecast as compared to the statistical model.

The coupled CFS model marginally but consistently outperforms the uncoupled GFS model by one to two days, indicating the limited improvement gained by the inclusion of the coupled air–sea interaction in the MJO forecast. This slight improvement may be related to a propagation barrier present in the simulation and forecast of the NCEP GFS and CFS models, as shown in this study and that of Seo et al. (2005, 2007). That is, the simulated or predicted MJO signal does not propagate across the Maritime Continent and the far western Pacific when the MJO develops over the Indian Ocean. Although, a recent study by Inness and Slingo (2006) suggests that poor representation of the Maritime Continent region in GCMs may inhibit MJO events from propagating into the west Pacific, other factors, including

convective parameterization and planetary boundary layer treatment, may also contribute to this problem. If this problem is resolved, then the MJO forecast skill will be enhanced and the effect of the air–sea interaction might be greater than the current results, since this air–sea interaction plays a critical role in the development and maintenance of the MJO.

Calculation for the 2005/06 version of the NCEP operational GFS model shows a skill of ~12–17 days for the winter season (Fig. 9). Although a strict comparison is not possible as a result of the different filtering method, the current operational GFS model forecast exhibits a skill for ~3–7 days longer than that of the previous NCEP GFS DERF using the 1996 GFS model (see Fig. 8 of Seo et al. 2005). The improved representation of the Maritime Continent region as a result of the much higher horizontal resolution and finer initial data might be an important factor for this improved skill.

As stated before, the CFS model yields a correlation skill of 0.5 for 17-day forecasts. This may cause an important ramification, since a proper representation of tropical intraseasonal convective forcing helps enhance the extended-range weather forecast skill in the extratropics (Ferranti et al. 1990). In particular, the possibility of improving the forecast in the western coast and mountain area in North America is increased—for example, during a "pineapple express" event, which is due to a storm event that brings (Hawaiian) tropical moisture air to the midlatitude area and results in heavy rainfall and severe weather. In addition, realistic MJO convection over the warm pool improves the simulation of northward propagating, stationary Rossby wave train (Matthews et al. 2004). Thus, the weather forecast in global areas will be improved by the enhanced MJO forecasting skill.

This work does not aim to improve the MJO forecast skill in the dynamical and statistical models but rather develop a consistent method to evaluate forecast skill from the two methods (i.e., dynamical and statistical) for real-time application. For an improved forecast scheme, a dynamical–statistical (i.e., CFS/GFS and lagged multiple regression) method is suggested. This hybrid scheme will overcome the difficulty in producing the longitudinal propagation across the Maritime Continent in GCMs and provide a better skill. The nonlinear neural network method is another candidate worthy of examination. Furthermore, if some component in the PC time series that represents convectively coupled ER and Kelvin waves not projected on the broadly defined MJO can be removed in real time, a much smoother PC index of the MJO will be produced, thereby providing longer autocorrelation time and thus higher forecast skill. More detailed studies on these issues are necessary.

Lastly, the current method for removing the ENSO-related interannual variability is based on linear regression. However, it is understood that the actual interaction between the MJO and ENSO is much more complicated. The two tend to have interrelated and nonlinear effects on each other. Furthermore, assessing the nonlinear effect of ENSO on the MJO is a challenging task. Therefore, an investigation of its effect on forecast skill is deferred to a future work.

Acknowledgments. The authors thank Drs. Matt Wheeler and Paul Roundy for their valuable comments and suggestions. This work was funded by the Korea Meteorological Administration Research and Development Program under Grant CATER 2007-4208 and the NOAA Climate Program Office under the Climate Variability and Predictability (CLIVAR) program. KH Seo would like to acknowledge the support from the Korea Institute of Science and Technology Information (KISTI).

APPENDIX

Forecast Equation Sets of PCRLAG for Each Forecast Horizon (Days Ahead)

$$\mathrm{PC}_1(t+h) = \sum_{j=1}^{15} a_j \mathrm{PC}_1(t-j+1) + \sum_{j=1}^{15} b_j \mathrm{PC}_2(t-j+1)$$

$$\mathrm{PC}_2(t+h) = \sum_{j=1}^{15} c_j \mathrm{PC}_1(t-j+1) + \sum_{j=1}^{15} d_j \mathrm{PC}_2(t-j+1)$$

Forecast horizon: h (days)				
1	a_j	1.452 −0.521 0.045 0.019 −0.019 0.005 −0.018 0.007 0.011 0.011 −0.064 0.048 −0.017 0.034 −0.024	c_j	−0.023 0.117 0.006 0.000 −0.077 0.061 −0.021 −0.001 0.014 −0.051 0.047 −0.034 0.019 −0.008 −0.002
	b_j	−0.050 −0.020 −0.022 0.027 0.036 −0.025 0.002 0.026 −0.012 −0.028 0.022 −0.018 0.004 0.013 0.000	d_j	1.406 −0.480 0.081 −0.036 −0.009 −0.015 0.013 0.023 −0.012 −0.007 −0.012 0.027 −0.019 0.035 −0.029

APPENDIX (*Continued*)

Forecast horizon: h (days)		$PC_1(t+h) = \sum_{j=1}^{15} a_j PC_1(t-j+1) + \sum_{j=1}^{15} b_j PC_2(t-j+1)$		$PC_2(t+h) = \sum_{j=1}^{15} c_j PC_1(t-j+1) + \sum_{j=1}^{15} d_j PC_2(t-j+1)$
2	a_j	1.589 −0.719 0.084 0.010 −0.020 −0.014 −0.017 0.021 0.025 −0.044 −0.047 0.053 0.011 0.019 −0.030	c_j	0.049 0.181 0.009 −0.079 −0.046 0.065 −0.031 0.011 −0.031 −0.025 0.033 −0.028 0.004 0.027
	b_j	−0.163 −0.027 −0.008 0.078 0.028 −0.034 0.028 0.025 −0.046 −0.018 0.014 −0.022 0.009 0.048 −0.020	d_j	1.497 −0.594 0.077 −0.059 −0.029 −0.008 0.041 0.018 −0.022 −0.024 0.010 0.017 0.020 −0.002 −0.024
3	a_j	1.594 −0.764 0.080 0.012 −0.033 −0.020 −0.003 0.037 −0.031 −0.019 −0.057 0.092 −0.008 0.009 −0.026	c_j	0.217 0.158 −0.065 −0.050 −0.050 0.061 −0.021 −0.034 −0.003 −0.043 0.039 −0.040 0.016 0.066 −0.076
	b_j	−0.336 0.038 0.031 0.077 0.026 −0.010 0.027 −0.008 −0.036 −0.029 0.014 −0.022 0.036 0.042 −0.029	d_j	1.507 −0.643 0.059 −0.080 −0.022 0.017 0.039 0.012 −0.038 −0.007 0.001 0.058 −0.021 0.023 −0.039
4	a_j	1.559 −0.791 0.082 −0.001 −0.025 −0.017 0.017 −0.019 −0.007 −0.020 −0.027 0.079 −0.022 0.017 −0.028	c_j	0.437 −0.002 −0.029 −0.050 −0.057 0.072 −0.069 −0.005 −0.019 −0.035 0.016 −0.019 0.052 0.018 −0.076
	b_j	−0.514 0.160 0.017 0.081 0.051 −0.009 −0.008 −0.002 −0.045 −0.028 0.017 0.004 0.038 0.027 −0.024	d_j	1.464 −0.670 0.036 −0.068 0.010 0.009 0.033 0.000 −0.023 −0.023 0.045 0.016 0.001 0.021 −0.047
5	a_j	1.486 −0.791 0.066 0.004 −0.006 −0.008 −0.036 0.004 −0.010 0.018 −0.046 0.072 −0.021 0.026 −0.033	c_j	0.597 −0.084 −0.020 −0.052 −0.047 0.022 −0.044 −0.019 −0.009 −0.053 0.019 0.029 0.007 0.005 −0.065
	b_j	−0.641 0.232 0.007 0.112 0.053 −0.041 −0.004 −0.017 −0.040 −0.024 0.043 −0.002 0.033 0.003 −0.003	d_j	1.366 −0.676 0.040 −0.030 0.011 −0.002 0.022 0.020 −0.040 0.017 0.008 0.032 0.000 0.009 −0.042
6	a_j	1.383 −0.784 0.068 0.021 0.013 −0.068 −0.008 0.001 0.025 0.003 −0.054 0.072 −0.012 0.023 −0.034	c_j	0.750 −0.171 −0.016 −0.038 −0.094 0.042 −0.058 −0.007 −0.027 −0.041 0.052 −0.005 −0.013 0.023 −0.069
	b_j	−0.743 0.285 0.028 0.117 0.019 −0.032 −0.023 −0.016 −0.034 0.007 0.038 −0.010 0.018 0.002 0.012	d_j	1.214 −0.630 0.068 −0.021 0.008 −0.018 0.042 0.004 −0.001 −0.025 0.031 0.026 −0.017 0.037 −0.056
7	a_j	1.242 −0.741 0.082 0.037 −0.036 −0.046 −0.008 0.035 0.009 −0.003 −0.050 0.080 −0.023 0.048 −0.051	c_j	0.888 −0.264 0.005 −0.085 −0.064 0.019 −0.045 −0.025 −0.016 0.002 0.002 −0.010 −0.024 0.085 −0.115
	b_j	−0.829 0.359 0.025 0.085 0.023 −0.043 −0.025–0.016 −0.001 0.006 0.028 −0.028 0.034 −0.031 0.046	d_j	1.038 −0.531 0.061 −0.013 −0.003 0.000 0.025 0.043 −0.041 −0.010 0.028 0.005 0.005 0.057 −0.079
8	a_j	1.083 −0.665 0.091 −0.016 −0.005 −0.052 0.031 0.018 0.000 0.003 −0.038 0.065 0.001 0.036 −0.054	c_j	1.001 −0.335 −0.036 −0.053 −0.076 0.022 −0.061 −0.012 0.026 −0.038 −0.019 −0.009 0.034 0.045 −0.118
	b_j	−0.869 0.400 −0.011 0.089 0.007 −0.041 −0.026 0.012 0.001 0.000 0.011 −0.014 0.012 −0.025 0.064	d_j	0.883 −0.456 0.050 −0.014 0.021 −0.015 0.061 0.003 −0.025 −0.014 0.011 0.021 0.030 0.026 −0.072
9	a_j	0.928 −0.577 0.032 0.013 −0.005 −0.015 0.017 0.007 0.004 0.015 −0.045 0.082 −0.005 0.023 −0.046	c_j	1.098 −0.453 −0.001 −0.063 −0.063 −0.004 −0.048 0.031 −0.015 −0.052 −0.032 0.059 −0.005 0.032 −0.109
	b_j	−0.876 0.386 −0.006 0.070 0.004 −0.038 0.001 0.010 −0.003 −0.013 0.024 −0.037 0.026 −0.032 0.081	d_j	0.735 −0.393 0.035 0.019 0.011 0.021 0.018 0.017 −0.029 −0.031 0.030 0.040 0.007 0.014 −0.056
10	a_j	0.791 −0.557 0.054 0.009 0.036 −0.030 0.009 0.010 0.015 0.005 −0.018 0.069 −0.018 0.034 −0.048	c_j	1.123 −0.484 −0.007 −0.049 −0.078 0.001 −0.005 −0.008 −0.029 −0.058 0.023 0.031 −0.024 0.048 −0.114
	b_j	−0.892 0.398 −0.024 0.064 0.001 −0.005 −0.003 0.002 −0.013 0.006 −0.004 −0.021 0.027 −0.042 0.099	d_j	0.584 −0.339 0.053 0.017 0.052 −0.021 0.030 0.011 −0.045 −0.013 0.052 0.012 0.002 0.009 −0.039

APPENDIX (*Continued*)

Forecast horizon: h (days)		$PC_1(t+h) = \sum_{j=1}^{15} a_j PC_1(t-j+1) + \sum_{j=1}^{15} b_j PC_2(t-j+1)$		$PC_2(t+h) = \sum_{j=1}^{15} c_j PC_1(t-j+1) + \sum_{j=1}^{15} d_j PC_2(t-j+1)$
11	a_j	0.614 −0.466 0.044 0.048 0.025 −0.039 0.014 0.020	c_j	1.132 −0.521 0.005 −0.062 −0.062 0.035 −0.042 −0.021
		0.003 0.031 −0.023 0.049 0.000 0.017 −0.038		−0.037 0.005 −0.014 0.017 0.004 0.007 −0.087
	b_j	−0.896 0.391 −0.028 0.057 0.029 −0.005 −0.012 −0.013	d_j	0.426 −0.249 0.038 0.063 0.014 −0.006 0.022 −0.007
		0.006 −0.017 0.010 −0.019 0.021 −0.041 0.109		−0.027 0.011 0.026 0.003 0.002 0.007 −0.025
12	a_j	0.447 −0.384 0.076 0.032 0.019 −0.035 0.028 0.007	c_j	1.112 −0.533 −0.008 −0.044 −0.017 −0.012 −0.050 0.029
		0.027 0.024 −0.031 0.059 −0.023 0.049 −0.053		0.023 −0.024 −0.035 0.048 −0.029 0.011 −0.071
	b_j	−0.900 0.392 −0.032 0.081 0.022 −0.010 −0.027 0.002	d_j	0.292 −0.188 0.072 0.030 0.029 −0.012 0.001 0.010
		−0.014 0.001 0.008 −0.022 0.023 −0.030 0.107		−0.004 −0.012 0.019 −0.002 −0.005 0.035 −0.034
13	a_j	0.286 −0.266 0.053 0.023 0.028 −0.022 0.018 0.030	c_j	1.076 −0.554 0.010 −0.001 −0.054 −0.028 −0.054 0.030
		0.018 0.014 −0.010 0.028 0.008 0.038 −0.056		−0.008 −0.038 −0.007 0.016 −0.036 0.058 −0.092
	b_j	−0.896 0.394 −0.005 0.070 0.011 −0.020 −0.013 −0.022	d_j	0.166 −0.088 0.028 0.052 0.022 −0.029 0.015 0.030
		0.006 0.003 0.001 −0.018 0.036 −0.041 0.112		−0.026 −0.017 0.015 −0.013 0.029 0.019 −0.029
14	a_j	0.171 −0.204 0.036 0.027 0.043 −0.033 0.043 0.020	c_j	1.006 −0.534 0.054 −0.040 −0.060 −0.038 0.009 −0.002
		0.007 0.033 −0.031 0.053 −0.003 0.036 −0.056		−0.024 −0.006 −0.041 0.011 −0.003 0.077 −0.120
	b_j	−0.880 0.422 −0.013 0.054 −0.005 −0.002 −0.037–0.007	d_j	0.090 −0.071 0.039 0.050 0.003 −0.011 0.032 0.005
		0.012 0.000 0.002 −0.002 0.026 −0.042 0.114		−0.030 −0.019 0.007 0.015 0.028 −0.006 −0.008
15	a_j	0.065 −0.158 0.035 0.041 0.034 −0.007 0.035 0.008	c_j	0.926 −0.463 0.011 −0.046 −0.064 0.021 −0.020 −0.019
		0.025 0.009 0.002 0.036 −0.004 0.033 −0.054		0.006 −0.037 −0.046 0.042 0.026 0.022 −0.100
	b_j	−0.825 0.409 −0.025 0.035 0.008 −0.023 −0.022 −0.005	d_j	0.005 −0.023 0.032 0.031 0.020 0.008 0.006 −0.002
		0.010 0.005 0.014 −0.007 0.022 −0.035 0.110		−0.032 −0.024 0.036 0.011 0.010 −0.009 0.009

REFERENCES

Carvalho, L. M. V., C. Jones, and B. Liebmann, 2004: The South Atlantic convergence zone: Intensity, form, persistence, and relationships with intraseasonal to interannual activity and extreme rainfall. *J. Climate,* **17,** 88–108.

Donald, A., H. Meinke, B. Power, A. de H. N. Maia, M. C. Wheeler, N. White, R. C. Stone, and J. Ribbe, 2006: Near-global impact of the Madden-Julian Oscillation on rainfall. *Geophys. Res. Lett.,* **33,** L09704, doi:10.1029/2005GL025155.

Ferranti, L., T. N. Palmer, F. Molteni, and E. Klinker, 1990: Tropical–extratropical interaction associated with the 30–60 day oscillation and its impact on medium and extended range prediction. *J. Atmos. Sci.,* **47,** 2177–2199.

Flatau, M., P. J. Flatau, P. Phoebus, and P. P. Niiler, 1997: The feedback between equatorial convection and local radiative and evaporative processes: The implications for intraseasonal oscillations. *J. Atmos. Sci.,* **54,** 2373–2386.

Fu, X., B. Wang, T. Li, and J. P. McCreary, 2003: Coupling between northward-propagating, intraseasonal oscillations and sea surface temperature in the Indian Ocean. *J. Atmos. Sci.,* **60,** 1733–1753.

Hendon, H. H., and B. Liebmann, 1990: The intraseasonal (30–50 day) oscillation of the Australian summer monsoon. *J. Atmos. Sci.,* **47,** 2909–2923.

——, and M. L. Salby, 1994: The life cycle of the Madden–Julian oscillation. *J. Atmos. Sci.,* **51,** 2225–2237.

——, and ——, 1996: Planetary-scale circulations forced by intraseasonal variations of observed convection. *J. Atmos. Sci.,* **53,** 1751–1758.

Higgins, R. W., and W. Shi, 2001: Intercomparison of the principal modes of interannual and intraseasonal variability of the North American monsoon system. *J. Climate,* **14,** 403–417.

——, J.-K. E. Schemm, W. Shi, and A. Leetmaa, 2000: Extreme precipitation events in the western United States related to tropical forcing. *J. Climate,* **13,** 793–820.

Hoffman, R. N., Z. Liu, J.-F. Louis, and C. Grassotti, 1995: Distortion representation of forecast errors. *Mon. Wea. Rev.,* **123,** 2758–2770.

Hsu, H.-H., and C.-H. Weng, 2001: Northwestward propagation of the intraseasonal oscillation in the western North Pacific during the boreal summer: Structure and mechanism. *J. Climate,* **14,** 3834–3850.

Inness, P. M., and J. M. Slingo, 2006: The interaction of the Madden-Julian Oscillation with the maritime continent in a GCM. *Quart. J. Roy. Meteor. Soc.,* **132,** 1645–1667.

Jones, C., and L. M. V. Carvalho, 2002: Active and break phases in the South American monsoon system. *J. Climate,* **15,** 905–914.

——, D. E. Waliser, J.-K. E. Schemm, and K.-M. Lau, 2000: Prediction skill of the Madden-Julian oscillation in dynamical extended range forecasts. *Climate Dyn.,* **16,** 273–289.

——, L. M. V. Carvalho, R. W. Higgins, D. E. Waliser, and J.-K. E. Schemm, 2004: A statistical forecast model of tropical intraseasonal convective anomalies. *J. Climate,* **17,** 2078–2095.

Kanamitsu, M., W. Ebisuzaki, J. Woollen, S.-K. Yang, J. J. Hnilo, M. Fiorino, and G. L. Potter, 2002: NCEP–DOE AMIP-II reanalysis (R-2). *Bull. Amer. Meteor. Soc.,* **83,** 1631–1643.

Kemball-Cook, S., and B. Wang, 2001: Equatorial waves and air–sea interaction in the boreal summer intraseasonal oscillation. *J. Climate,* **14,** 2923–2942.

——, ——, and X. Fu, 2002: Simulation of the intraseasonal oscillation in the ECHAM-4 model: Impact of coupling with an ocean model. *J. Atmos. Sci.,* **59,** 1433–1453.

Kessler, W., and R. Kleeman, 2000: Rectification of the Madden–Julian oscillation into the ENSO cycle. *J. Climate,* **13,** 3560–3575.

Kousky, V. E., and M. T. Kayano, 1994: Principal modes of outgoing longwave radiation and 250-mb circulation for the South American sector. *J. Climate,* **7,** 1131–1143.

Krishnamurti, T. N., D. K. Oosterhof, and A. V. Mehta, 1988: Air–sea interaction on the time scale of 30 to 50 days. *J. Atmos. Sci.,* **45,** 1304–1322.

Lau, K.-M., and P. H. Chan, 1986: Aspects of the 40–50 day oscillation during the northern summer as inferred from outgoing longwave radiation. *Mon. Wea. Rev.,* **114,** 1354–1367.

Liebmann, B., and C. A. Smith, 1996: Description of a complete (interpolated) outgoing longwave radiation dataset. *Bull. Amer. Meteor. Soc.,* **77,** 1275–1277.

Lin, J.-L., and Coauthors, 2006: Tropical intraseasonal variability in 14 IPCC AR4 climate models. Part I: Convective signals. *J. Climate,* **19,** 2665–2690.

Lo, F., and H. H. Hendon, 2000: Empirical extended-range prediction of the Madden–Julian oscillation. *Mon. Wea. Rev.,* **128,** 2528–2543.

Madden, R. A., and P. R. Julian, 1994: Observations of the 40–50-day tropical oscillation—A review. *Mon. Wea. Rev.,* **122,** 814–837.

Maharaj, E. A., and M. C. Wheeler, 2005: Forecasting an index of the Madden-Julian oscillation. *Int. J. Climatol.,* **25,** 1611–1618.

Maloney, E. D., and D. L. Hartmann, 2000: Modulation of eastern North Pacific hurricanes by the Madden–Julian oscillation. *J. Climate,* **13,** 1451–1460.

Matthews, A. J., B. J. Hoskins, J. Slingo, and M. Blackburn, 1996: Development of convection along the SPCZ within a Madden-Julian oscillation. *Quart. J. Roy. Meteor. Soc.,* **122,** 1473–1498.

——, ——, and M. Masutani, 2004: The global response to tropical heating in the Madden-Julian oscillation during the northern winter. *Quart. J. Roy. Meteor. Soc.,* **130,** 1911–2011.

McPhaden, M. J., 1999: Genesis and evolution of the 1997-98 El Niño. *Science,* **283,** 950–954.

——, 2004: Evolution of the 2002/03 El Niño. *Bull. Amer. Meteor. Soc.,* **85,** 677–695.

Mo, K. C., 2000: Intraseasonal modulation of summer precipitation over North America. *Mon. Wea. Rev.,* **128,** 1490–1505.

——, and W. R. Higgins, 1998: Tropical convection and precipitation regimes in the western United States. *J. Climate,* **11,** 2402–2423.

Newton, H. J., 1988: *TIMESLAB: A Time Series Analysis Laboratory*. Wadsworth, 623 pp.

Pacanowski, R. C., and S. M. Griffies, 1998: MOM 3.0 manual. NOAA/Geophysical Fluid Dynamics Laboratory, 680 pp.

Reynolds, R. W., N. A. Rayner, T. M. Smith, D. C. Stokes, and W. Wang, 2002: An improved in situ and satellite SST analysis for climate. *J. Climate,* **15,** 1609–1625.

Roundy, P. E., C. J. Schreck III, and M. A. Janiga, 2009: Contributions of convectively coupled equatorial Rossby waves and Kelvin waves to the real-time multivariate MJO indices. *Mon. Wea. Rev.,* **137,** 363–372.

Saha, S., and Coauthors, 2006: The NCEP Climate Forecast System. *J. Climate,* **19,** 3483–3517.

Seo, K.-H., and Y. Xue, 2005: MJO–related oceanic Kelvin waves and the ENSO cycle: A study with the NCEP Global Ocean Data Assimilation System. *Geophys. Res. Lett.,* **32,** L07712, doi:10.1029/2005GL022511.

——, J.-K. E. Schemm, C. Jones, and S. Moorthi, 2005: Forecast skill of the tropical intraseasonal oscillation in the NCEP GFS dynamical extended range forecasts. *Climate Dyn.,* **25,** 265–284.

——, ——, W. Wang, and A. Kumar, 2007: The boreal summer intraseasonal oscillation simulated in the NCEP Climate Forecast System (CFS): The effect of sea surface temperature. *Mon. Wea. Rev.,* **135,** 1807–1827.

Shinoda, T., H. H. Hendon, and J. Glick, 1998: Intraseasonal variability of surface fluxes and sea surface temperature in the tropical western Pacific and Indian Oceans. *J. Climate,* **11,** 1685–1702.

Van den Dool, H., 2007: *Empirical Methods in Short-Term Climate Prediction*. Oxford University Press, 215 pp.

Waliser, D. E., C. Jones, J.-K. E. Schemm, and N. E. Graham, 1999: A statistical extended-range tropical forecast model based on the slow evolution of the Madden–Julian oscillation. *J. Climate,* **12,** 1918–1939.

——, K. M. Lau, W. Stern, and C. Jones, 2003: Potential predictability of the Madden–Julian oscillation. *Bull. Amer. Meteor. Soc.,* **84,** 33–50.

Wang, B., and X. Xie, 1998: Coupled modes of the warm pool climate system. Part I: The role of air–sea interaction in maintaining Madden–Julian oscillation. *J. Climate,* **11,** 2116–2135.

Wang, W., S. Saha, H.-L. Pan, S. Nadiga, and G. White, 2005: Simulation of ENSO in the new NCEP Coupled Forecast System Model (CFS03). *Mon. Wea. Rev.,* **133,** 1574–1593.

Wheeler, M., and G. N. Kiladis, 1999: Convectively coupled equatorial waves: Analysis of clouds and temperature in the wavenumber–frequency domain. *J. Atmos. Sci.,* **56,** 374–399.

——, and K. M. Weickmann, 2001: Real-time monitoring and prediction of modes of coherent synoptic to intraseasonal tropical variability. *Mon. Wea. Rev.,* **129,** 2677–2694.

——, and H. H. Hendon, 2004: An all-season real-time multivariate MJO index: Development of an index for monitoring and prediction. *Mon. Wea. Rev.,* **132,** 1917–1932.

Whitaker, J. S., and K. M. Weickmann, 2001: Subseasonal variations of tropical convection and week-2 prediction of wintertime western North American rainfall. *J. Climate,* **14,** 3279–3288.

Woolnough, S. J., J. M. Slingo, and B. J. Hoskins, 2000: The relationship between convection and sea surface temperature on intraseasonal timescales. *J. Climate,* **13,** 2086–2104.

Yasunari, T., 1980: A quasi-stationary appearance of the 30-40 day period in the cloudiness fluctuations during the summer monsoon over India. *J. Meteor. Soc. Japan,* **58,** 225–229.

Zhang, C., 1996: Atmospheric intraseasonal variability at the surface in the tropical western Pacific Ocean. *J. Atmos. Sci.,* **53,** 739–758.

——, and J. Gottschalck, 2002: SST anomalies of ENSO and the Madden–Julian oscillation in the equatorial Pacific. *J. Climate,* **15,** 2429–2445.